RESEARCH PAPER

Template synthesis of graphene/polyaniline hybrid hollow microspheres as electrode materials for high-performance supercapacitor

Bin Mu · Wenbo Zhang · Aiqin Wang

Abstract Graphene/polyaniline hybrid hollow microspheres are prepared via combining layer-by-layer assembly technique with in situ chemical oxidative polymerization after etching the templates for high-performance supercapacitor application. The hollow structure is characterized by transmission electron microscopy indicating that the inner diameter of the hollow microspheres is about 2.0 μm. The electrochemical tests show that the specific capacitance of the graphene/polyaniline hybrid hollow microsphere electrode materials can reach about 633 F g^{-1} in a 1.0 M H$_2$SO$_4$ electrolyte. It is higher than that of polyaniline hollow microspheres (389 F g^{-1}), pure polyaniline particles (152 F g^{-1}), and graphene/sodium alginate hollow microspheres (16 F g^{-1}). The high specific capacitance might be attributed to the unique hollow structure and the synergistic effect of the hybrid shell. Their unique structure provides an enhanced surface-to-volume ratio and reduced transport lengths for both mass and charge transport. Furthermore, graphene/polyaniline hybrid hollow microsphere electrode materials display good cycle stability with 92 % of its original specific capacitance after 1,000 cycles by continuous cyclic voltammetric scans at 80 mV s^{-1}.

Introduction

With the rapid development of the global economy, the depletion of fossil fuels and the environmental contamination is driving scientists and engineers to develop renewable, highly efficient methods of creating and storing energy without damaging the environment. It has inspired recent advances in new clean sources as well as new technologies associated with electrochemical energy storage and conversion including batteries, solar cells, fuel cells, and supercapacitors (Kamat 2007; Zhong et al. 2008; Etacheri et al. 2011; Hadjipaschalis et al. 2009). In recent years, supercapacitors have increasingly attracted research attention due to their high power density, long lifecycle, and bridging function for the power/energy gap between traditional dielectric capacitors with high power output and batteries/fuel cells with high energy storage (Balducci et al. 2007). However, the disadvantages of low energy density and high production cost have also restricted the rapid development of supercapacitors. It is urgent to make greater efforts in

B. Mu · W. Zhang · A. Wang (✉)
Center of Eco-material and Green Chemistry, Lanzhou Institute of Chemical Physics, Chinese Academy of Sciences, Lanzhou 730000, China
e-mail: aqwang@licp.cas.cn

W. Zhang
Graduate University of the Chinese Academy of Sciences, Beijing 100049, China

the design and synthesizing of novel materials for supercapacitor electrodes to resolve above obstacle.

Hollow micro-/nano-structured materials have been acknowledged as a promising material for applications in energy-related systems. Their unique structure possesses more advantages in an enhanced surface-to-volume ratio and reduced transport lengths for both mass and charge transport (Lai et al. 2012). Three distinct synthetic strategies were developed to prepare the hollow micro-/nano-structured materials. Hard-template methods make use of "rigid" materials as templates, such as polystyrene (Mu et al. 2012), silica (Huang et al. 2011), poly(L-lactide) fibers (Dong et al. 2004), etc. The soft template synthesis, also named self-assembly method, employs liquid droplets or micelles as templates by microemulsion polymerization and reversed-microemulsion polymerization in which surfactants are involved (Jang and Yoon 2003). In addition, some hollow structure was prepared using template-free methods, which allow to materials to self-assemble into the desired structures (Chiou et al. 2007). Hard-template methods, by contrast, have been widely adopted for the preparation of hollow structure materials since they are straightforward to apply and have obvious advantages for controlling the size, shape, and structure of shell (Lou et al. 2008).

The layer-by-layer (LBL) adsorption technique offers an easy and inexpensive process for multilayer formation and allows a variety of materials to be incorporated within the film structures. One of the most outstanding strategy modifications for LBL assembly preparation involves the alternating adsorption of charged species onto oppositely charged three-dimensional spherical colloid or one-dimension tube templates using intermolecular interactions as the driving force, and subsequently removes the templates via chemical or thermal means to obtain hollow microspheres or tubes (Caruso 2000; Ariga et al. 2007; Angelatos and Katagiri 2006; Peyratout and Dähne 2004; Liu et al. 2008). It permits unprecedented control over hollow structure properties (size, composition, thickness, permeability, and function) through the choice of the sacrificial templates and the shell components. Therefore, various types of carbon-based hollow microspheres by LBL colloid-templating technique have been prepared (Hong et al. 2010; Tang et al. 2009; Shi et al. 2008). However, very few studies concerning the electrochemical property of carbon-based hollow
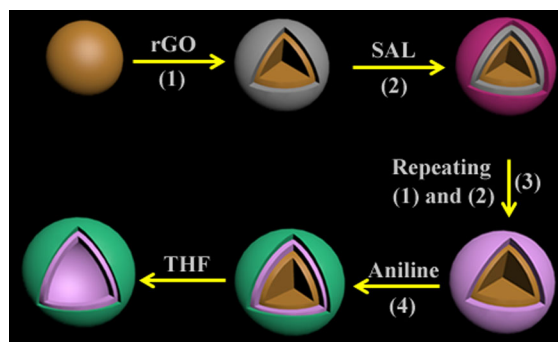
Scheme 1 Illustration of the preparation of graphene/PAn hybrid hollow microspheres combining LBL assembly technique with in situ chemical oxidative polymerization

microspheres used as electrode materials have been reported (Han et al. 2012). It might be attributed to the fact that the charges physically stored on the carbon particles in porous electrode layers are unfortunately limited, so supercapacitors used carbon-based materials as electrodes have a limited specific capacitance and a low energy density (Zhu et al. 2011). Advanced approaches to increase the energy density of carbon-based materials supercapacitors are to hybridize the electrode materials via loading or encapsulation transition metal oxide or conductive polymer to obtain the binary or ternary hybrid electrochemical active materials (Zolfaghari et al. 2013; Yu et al. 2011a, b; Bose et al. 2012; Jiang et al. 2012; Li et al. 2012). It allows the systems to benefit from the synergetic merits of both electrical double-layer capacitance and pseudocapacitance, resulting in supercapacitors with high performance.

In this paper, the graphene/polyaniline hollow microsphere hybrid structures have been fabricated based on the polystyrene sulfonate microsphere (PSS) templates after etching the templates. As illustrated in Scheme 1, the construction of the hybrid hollow structure mainly involves the LBL assembly of amino functionalized reduced graphene oxide (rGO) and sodium alginate (SAL) on the PSS templates, the in situ chemical oxidative polymerization of aniline, and the etching of PSS templates using THF. In addition, the influence of the hollow structure and the synergy of components of the hybrid shell on the electrochemical property were investigated in detail. It suggested that rGO/PAn HM hybrid electrode materials might have potential applications in high-performance energy storage devices.

Experimental

Materials

Styrene (St, analytical reagent, Tianjin Chemicals Co. Ltd., China) was purified by removing inhibitor through an aluminum oxide column and then stirred with CaH_2 overnight and distilled under reduced pressure before use. Aniline, ammonium peroxydisulfate (APS) and other chemicals were analytical grade and used without further purification. The ultrapure water (resistivity = 18.25 MΩ cm) was used throughout.

Preparation of amino functionalized reduced graphene

Graphite oxide (GO) was synthesized from nature graphite using a modified Hummers method as originally presented by Kovtyukhova et al. (1999). 50 mg of benzidine hydrochloride was added into 200 mL of water containing as-prepared GO (100 mg), and stirred for 24 h at 60 °C. Then hydrazine monohydrate solution (2 M) was added to obtain amino functionalized reduced rGO, which was dispersed in 20 mL of water to obtain the dispersion of rGO for the next adsorption.

Preparation of rGO/PAn hybrid shell coated PSS templates

The PSS templates prepared according to the methods as reported in our previous work (Mu et al. 2013). Firstly, 20 mL of St and 3.2 g of PVP were added to 125 mL of absolute ethanol, and then 0.145 g of azodiisobutyronitrile was added to the reaction vessel with vigorous stirring under nitrogen. The polymerization was continued for 24 h at 80 °C, and the white product was washed by repeated centrifugation and dried in a vacuum oven at 50 °C. Secondly, the white powder was dispersed in concentrated sulfuric acid with the aid of magnetic stirring at 45 °C for 3 h to complete the sulfonation reaction. The obtained PSS templates were dried in a vacuum oven at 40 °C after being washing with a large excess of water.

The LBL assembly technique was applied for the preparation of the hybrid shell composed of rGO and SAL encapsulated PSS by electrostatic interaction between the amino groups of rGO and the carboxyl groups of SAL. Firstly, the as-prepared rGO solution (2 mL) was added into 100 mL of deionized water containing 0.1 g of PSS under stirring for 30 min to complete the adsorption of rGO, and then followed by being centrifuged and washed three times with water to obtain rGO encapsulated PSS. Next, 10 mL of SAL solution (5 mg/mL) was added into 100 mL of water containing rGO encapsulated PSS, and the products were centrifuged and washed three times with water after being stirred for 30 min. Then, rGO and SAL were alternately deposited a further two times and five time onto the PSS templates, and the products were labeled as PSS@(rGO/SAL)$_3$ and PSS@(rGO/SAL)$_6$, respectively. Then, the coating of polyaniline (PAn) on the rGO/SAL hybrid multilayer encapsulated PSS was completed by in situ chemical oxidative polymerization using aniline as the monomer and APS as the oxidant in 1 M HCl solution, and the mole ratio of aniline to APS was 4:1. The products were washed with water and separated by centrifugation until a neutral pH was reached. The resulting products were dried under vacuum at 40 °C and labeled as PSS@(rGO/SAL)$_3$/PAn, PSS@(rGO/SAL)$_6$/PAn$_1$ and PSS@(rGO/SAL)$_6$/PAn$_2$ corresponding to the addition of 2, 1, and 2 mL aniline, respectively.

Preparation of rGO/PAn hollow microspheres (rGO/PAn HM)

The PSS templates were removed using THF to obtain the rGO/PAn hollow microspheres ((rGO/SAL)$_3$/PAn HM, (rGO/SAL)$_6$/PAn$_1$ HM and (rGO/SAL)$_6$/PAn$_2$ HM) after being centrifuged, washed and dried, respectively. The absence of the templates was confirmed by mixing the final centrifugate with three times volume water, ensuring the absence of any precipitate. For comparison, PAn nanoparticles, (rGO/SAL)$_3$ hollow microspheres ((rGO/SAL)$_3$ HM) and PAn hollow microspheres (PAn HM) were also prepared.

Characterizations

Bruker IFS 66 v/s IR spectrometer (Bruker, Karlsruhe, Germany) was used for the Fourier transform infrared (FTIR) spectroscopy analysis. Elemental analysis (EA) of the samples was performed on Elementar vario EL instrument (ELEMENTAR Company, Germany). The morphologies of the samples were

characterized with a JEM-1200 EX/S TEM (JEOL, Tokyo, Japan) and S-4800 field emission SEM (HIT-ACHI, Tokyo, Japan), respectively. The electrical conductivities of the samples were measured using RTS-2 four-point probe meter (Guangzhou four-point probe meter Electronic Technology Co., Ltd) at ambient temperature.

The working electrodes were fabricated with the mixture containing the obtained active materials, carbon black, and polyvinylidenefluoride with mass ratio of 80:15:5 to make homogeneous mixture in *N,N*-dimethylformamide (Zhang et al. 2010a). Then, the slurry was uniformly laid on stainless steel mesh that used as a current collector and then dried at 50 °C for 24 h. The electrochemical behavior of the composite electrodes was evaluated by cyclic voltammetry (CV), galvanostatic charge–discharge, and electrochemical impedance spectroscopy (EIS) using a CHI660B electrochemical working station. All electrochemical experiments were carried out in a three-electrode glass cell, a platinumcounter electrode, and a standard calomel reference electrode in 1.0 M H_2SO_4 electrolyte solution.

Results and discussion

The TEM image of reduced graphene is shown in Fig. 1a, and it can be seen that graphene sheets exhibit a laminar structure, indicating the formation of the well-exfoliated graphene sheets. The diameter of graphene sheets is about 1.0 μm by comparison with scale shown in the TEM image. A typical TEM image of PSS microspheres is given in Fig. 1b. The microspheres are spherical in shape and monodisperse in size with a diameter of about 2.0 μm. It can been seen from Fig. 1c, d that the surface of PSS microspheres becomes rough after alternating adsorption three times of rGO and SAL compared with the primitive PSS. It can clearly observe the graphene sheets on the surface of PSS and the diameter of PSS@(rGO/SAL)$_3$ is about 2.2 μm. It indicates that the rGO/SAL hybrid shells are successfully adsorbed onto the surface of PSS. As shown in Fig. 1e, the diameter of PSS@(rGO/SAL)$_6$ is about 2.3 μm after alternating deposition six times of rGO and SAL. It indicates that the diameter of the rGO/SAL hybrid shells coated PSS increases with the increase in the number of the adsorption of rGO and SAL. The diameters of PSS@(rGO/SAL)$_6$/PAn$_1$ and

PSS@(rGO/SAL)$_6$/PAn$_2$ are around 2.4 and 2.6 μm with a typical core–shell morphology as shown in Fig. 1f, g, respectively. It shows that the PAn particles form on the surface of the rGO/SAL hybrid shells coated PSS templates during the process of chemical oxidative polymerization. In addition, it also can roughly calculate the thickness of PAn layer in PSS@(rGO/SAL)$_6$/PAn$_1$ and PSS@(rGO/SAL)$_6$/PAn$_2$ are about 100 and 300 nm, respectively. In other word, the diameters of the rGO/PAn hybrid shell encapsulated PSS increases with the increase in the addition of aniline. The PSS templates can decompose into their constituent oligomers upon treatment with THF to be removed, and the TEM image provides direct evidence of the hollow structure. It can be observed from Fig. 1h that the diameter of the (rGO/SAL)$_6$/PAn$_2$ HM is about 2.6 μm, and the inner diameter is around 2.0 μm, which is consentient with the diameter of the primitive PSS templates.

The surface morphology analysis of PSS@(rGO/SAL)$_3$ and PSS@(rGO/SAL)$_6$/PAn$_2$ are investigated by SEM. As shown in Fig. 2a, the surface of PSS@(rGO/SAL)$_3$ presents the typical laminar structure, indicating graphene sheets have been successfully adsorbed on to the surface of PSS by LBL adsorption technique. After coating PAn on the rGO/SAL hybrid shells coated PSS, the SEM image of PSS@(rGO/SAL)$_6$/PAn$_2$ indicates a more coarse surface with a diameter of 2.6 μm (Fig. 2b), which is almost consentient with the result of TEM.

Figure 3 shows the FTIR spectra of PSS@((rGO/SAL)$_3$, PSS@(rGO/SAL)$_6$/PAn$_2$, and (rGO/SAL)$_6$/PAn$_2$ HM. The FTIR spectrum of PSS@((rGO/SAL)$_3$ reveals that the well-defined characteristic adsorption bands of benzene ring at 3080, 3060, and 3020 cm^{-1} (C–H, stretching vibration), 1601, 1492, and 1452 cm^{-1} (C=C, stretching vibration), 698 cm^{-1} (out of plane blending vibration, δring). After coating PAn, the adsorption bands of N–H stretching band at 3,436 cm^{-1}, C=C (quinoid, Q) stretching band at 1,580 cm^{-1}, C=C stretching band in the benzenoid ring at 1,481 cm^{-1}, the aromatic C–N stretching band at 1,301 cm^{-1}, the N=Q=N at 1,140 cm^{-1}, and γ(C–H) of 1,4-disubstituted aromatic ring at 814 cm^{-1} can be observed (Li et al. 2011a, b, c; Park et al. 2003). In addition, the characteristic adsorption bands of the templates disappears after etching the PSS cores as shown in the FTIR spectrum of (rGO/SAL)$_6$/PAn$_2$
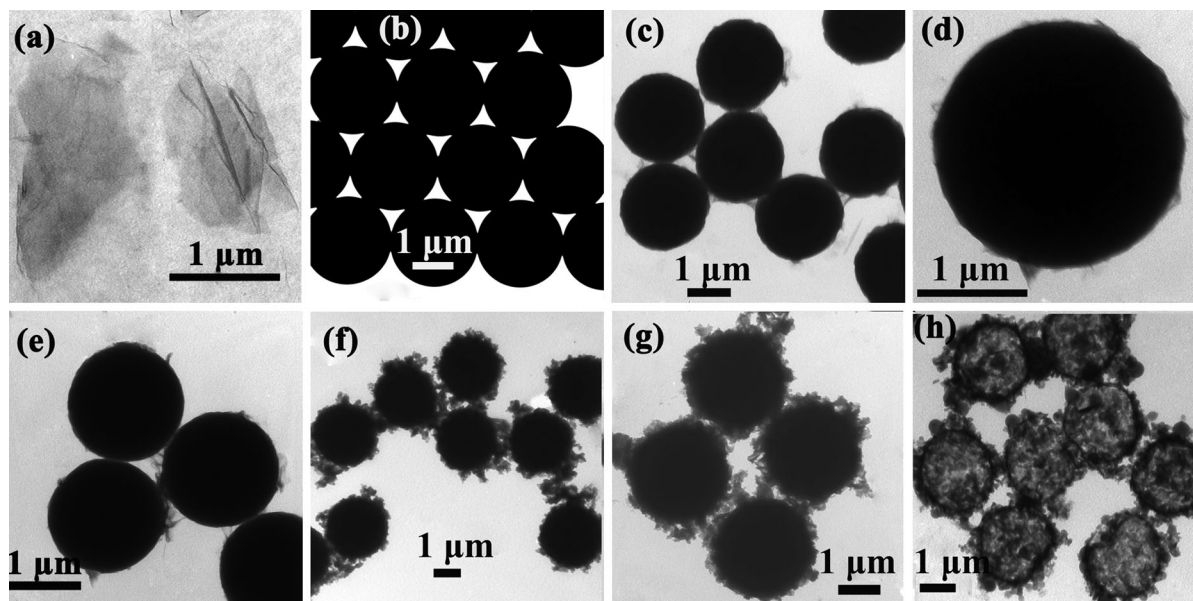
Fig. 1 TEM images of **a** rGO, **b** PSS templates, **c**, **d** PSS@(rGO/SAL)$_3$, **e** PSS@(rGO/SAL)$_6$, **f** PSS@(rGO/SAL)$_6$/PAn$_1$, **g** PSS@(rGO/SAL)$_6$/PAn$_2$, **h** (rGO/SAL)$_6$/PAn$_2$ HM
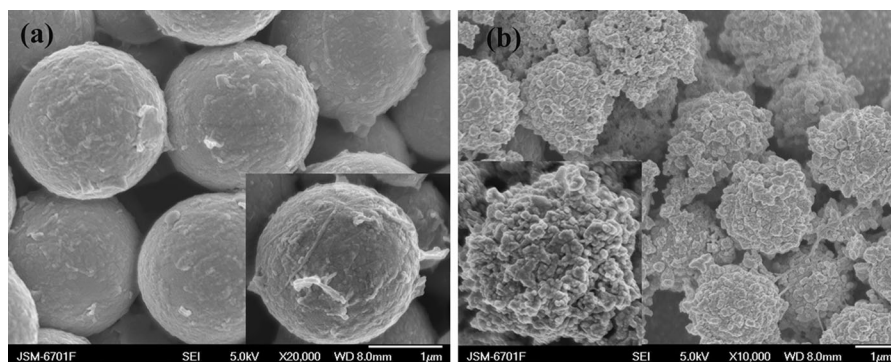

Fig. 2 SEM images of **a** PSS@(rGO/SAL)$_3$, and **b** PSS@(rGO/SAL)6/PAn$_2$

HM, and it indicates that PSS templates are completely removed.

Figure 4 shows that the UV–vis spectra of (rGO/SAL)$_3$ HM and (rGO/SAL)$_6$/PAn$_2$ HM. It can be found that two broad absorption bands at around 320–500 nm and 820 nm from the UV–vis spectrum of (rGO/SAL)$_6$/PAn$_2$ HM, respectively. The first adsorption band is attributed to the π–π* transition of benzenoid rings, while the adsorption band at 820 nm is ascribed to the protonation of the imine sites of PAn, which originates from the polaron band transition (Stejskal et al. 1993; Huang et al. 2003). Furthermore, a tail of the broad band at 820 nm

extends into the near infrared spectrum region, which is an indication of the emeraldine salt oxidation state of PAn (Chiou and Epstein 2005). By contrast, no adsorption peak presented in the spectrum of (rGO/SAL)$_3$ HM.

Compared with bulk PAn particles, the obtained rGO/PAn HM would be expected to be a promising candidate for the construction of high-performance supercapacitors due to the unique properties arising from their hollow structure and the synergistic effect of hybrid shell: (i) short path lengths for the transport of ions; (ii) better accommodation of the strain caused by electrochemical reaction; (iii) mixed conductive
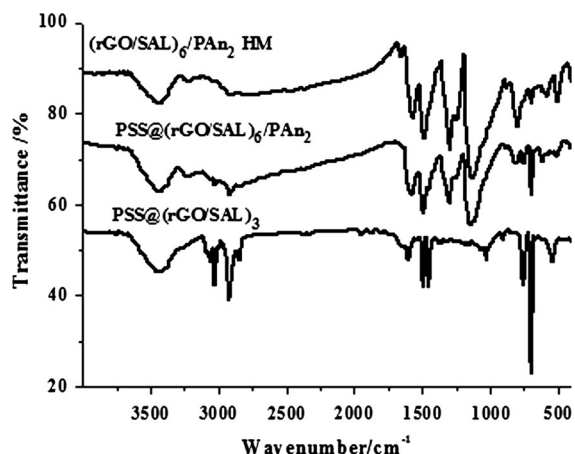
Fig. 3 The FTIR spectra of PSS@(rGO/SAL)$_3$, PSS@(rGO/SAL)$_6$/PAn$_2$, and (rGO/SAL)$_6$/PAn$_2$ HM
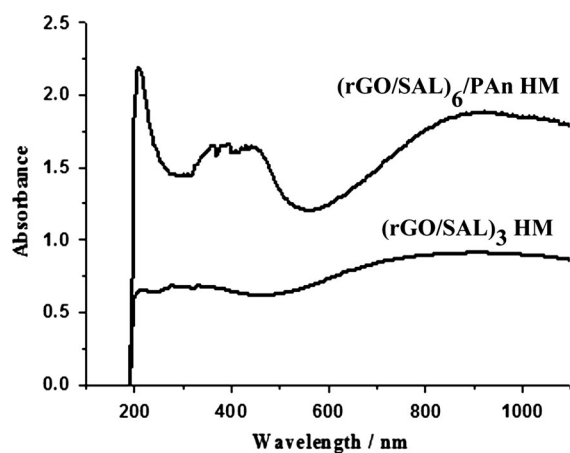

Fig. 4 The UV–vis spectra of (rGO/SAL)$_3$ HM and (rGO/SAL)$_6$/PAn$_2$ HM

mechanism of both electronic and ionic conductivity, which lowers the interfacial impedance between electrodes and electrolyte; (iv) light weight and large ratio of specific discharge power to weight. Therefore, the obtained rGO/PAn HM was used to fabricate supercapacitor electrodes and characterized with cyclic voltammetry (CV), galvanostatic charge/discharge and impedance measurements to investigate the potential application in electrochemical energy storage.

Figure 5a presents the CV curves of PAn particles, PAn HM, (rGO/SAL)$_3$ HM, (rGO/SAL)$_6$/PAn$_1$ HM, and (rGO/SAL)$_6$/PAn$_2$ HM at a scan rate of 10 mV s^{-1} in 1.0 M H$_2$SO$_4$ aqueous solution. The

CV curves of the samples containing PAn presents a pair of redox peaks in the range of −0.3–0.8 V related to two redox processes: leucoemeraldine to emeraldine salt and emeraldine salt to the pernigraniline state compared with (rGO/SAL)$_3$ HM (Zhang et al. 2010b). All of the rGO/PAn HM electrodes shows much larger integrated areas than the PAn particles, PAn HM, and (rGO/SAL)$_3$ HM electrodes, exhibiting a higher specific capacitance. This might be attributed to the unique hollow structure and the synergistic effect between rGO and PAn of hybrid shell. The hollow structure provides an enhanced electrode/electrolyte interface area, providing high electroactive regions and short diffusion lengths, which can ensure PAn quickly and fully participate in the charge–discharge reaction and a high utilization of electroactive materials (Wu et al. 2010). At the same time, rGO in the hybrid shell can offer highly conductive pathways by bridging the adjacent individual PAn chain, thus facilitating rapid transport of the electrolyte ions in the electrode during rapid charge–discharge process (Chen et al. 2011a). Therefore, rGO/PAn HM electrodes can drastically reduce the diffusion length, leading to the improvement of the electrochemical properties. According to the results of EA, it can calculate the content of PAn in (rGO/SAL)$_3$/PAn HM, (rGO/SAL)$_6$/PAn$_1$ HM, and (rGO/SAL)$_6$/PAn$_2$ HM is 1.54, 1.16, and 1.48 g/g, respectively. Therefore, it also can be found that the integrated areas of as-prepared rGO/PAn HM electrodes gradually increases with the increase in the adsorption numbers of rGO and the content of PAn, indicating that (rGO/SAL)$_6$/PAn$_2$ HM has high capacitance compared with that of (rGO/SAL)$_3$/PAn HM and (rGO/SAL)$_6$/PAn$_1$ HM. It might be ascribed to the fact that the content of electroactive materials of hybrid shell increased with the increase in the adsorption number of rGO and the initial concentration of aniline. However, the over-thick PAn layer can decrease the specific capacitance and capacitance retention of the electrode materials (Lei et al. 2010). It was mainly ascribed to the fact that the increase in the thickness of PAn layer hindered the charge transfer between the electrode materials and the current collector, and increased the diffusion resistance of electrolyte ions in the electrode. Furthermore, the increase in the thickness of PAn layer led to less access of electrolyte ions to the active sites of PAn layers and a reduced contribution of pseudo-capacitance from the redox reaction of PAn at the interface of
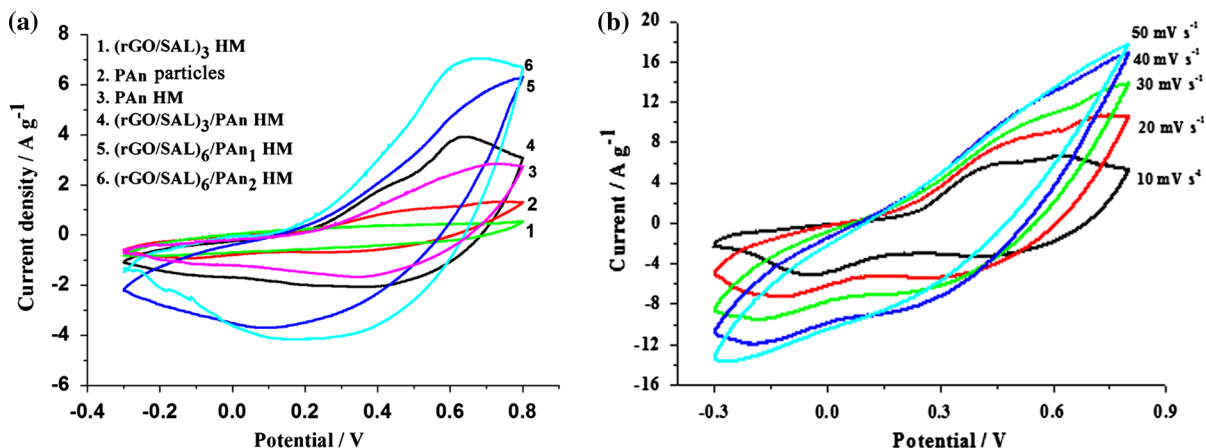
Fig. 5 a Cyclic voltammogram curves of PAn particles, PAn HM, (rGO/SAL)$_3$/PAn HM, (rGO/SAL)$_6$/PAn$_1$ HM, and (rGO/SAL)$_6$/PAn$_2$ HM electrodes at 10 mV s^{-1} in 1.0 M H$_2$SO$_4$

solution. b Scan rate dependence of (rGO/SAL)$_6$/PAn$_2$ HM electrode in 1.0 M H$_2$SO$_4$ solution

the electrolyte/electrode, suggesting low utilization efficiency of the PAn. Figure 5b shows the CV curves of (rGO/SAL)$_6$/PAn$_2$ HM at different scan rates, indicating that the electrode materials keep good electrochemical property and quickly ion exchange in the process of charge–discharge. However, the effective interaction between the ions and the electrode decreases greatly with the increase in the scan rate.

The galvanostatic charge–discharge measurements of the pure PAn particles, PAn HM, (rGO/SAL)$_3$ HM, (rGO/SAL)$_3$/PAn HM, (rGO/SAL)$_6$/PAn$_1$ HM, and (rGO/SAL)$_6$/PAn$_2$ HM electrodes were carried out in 1.0 M H$_2$SO$_4$ aqueous solution between −0.3 and 0.8 V at a current density of 10 mA cm^{-2}. As shown in Fig. 6a, the charge curves of all of the electrodes are almost symmetric to the corresponding discharge counterparts with a slight curvature, especially for the rGO/PAn HM electrodes. It indicates that the energy storage of the as-prepared rGO/PAn HM electrodes is composed of double-layer capacitance and Faradaic pseudocapacitance. The IR drop at the beginning of the discharging process is indicative of the internal resistance of the electrode. Although the charge–discharge curves of PAn HM electrode maintain the similar shape of the rGO/PAn HM electrodes, the IR drop of the (rGO/SAL)$_6$/PAn$_2$ HM electrode is much smaller than that of pure PAn particles, PAn HM, (rGO/SAL)$_3$/PAn HM, and (rGO/SAL)$_6$/PAn$_1$ HM electrodes, indicating that the internal resistance of PAn is much higher than that of the hybrid materials. Low internal resistance is of great importance in

energy storage devices, since less energy will be wasted to produce unwanted heat during charge–discharge processes (Wu et al. 2010; Fan et al. 2013). The leucoemeraldine or pernigraniline form of PAn is an insulator, so the electrode materials based on pure PAn particles, PAn HM, (rGO/SAL)$_3$/PAn HM has a large internal resistance as it is fully charged or discharged due to the high content of PAn.

To compare the discharge curves of all of the charge–discharge curves as shown in Fig. 6a, the (rGO/SAL)$_6$/PAn$_2$ HM electrode exhibits a much longer discharge time, which is consistent with the specific capacitance behavior, because the discharging time is directly proportional to the specific capacitance of the electrode materials (Kim et al. 2013). The specific capacitance (C_m) and energy density (E) can be calculated according to the following equations:

$$C_m = \frac{I\Delta t}{\Delta V m}$$

$$E = \frac{1}{2}C_m \Delta V^2$$

where I is the charge–discharge current, Δt is the discharge time obtained from galvanostatic charge–discharge curves of electrode materials, ΔV is the electrochemical window, and m is the mass of active material within the electrode. It can be calculated that the specific capacitance of (rGO/SAL)$_3$/PAn HM, (rGO/SAL)$_6$/PAn$_1$ HM, and (rGO/SAL)$_6$/PAn$_2$ HM is 528, 629, and 633 F g^{-1}, respectively. It was higher than that of PAn HM (389 F g^{-1}), pure PAn particles
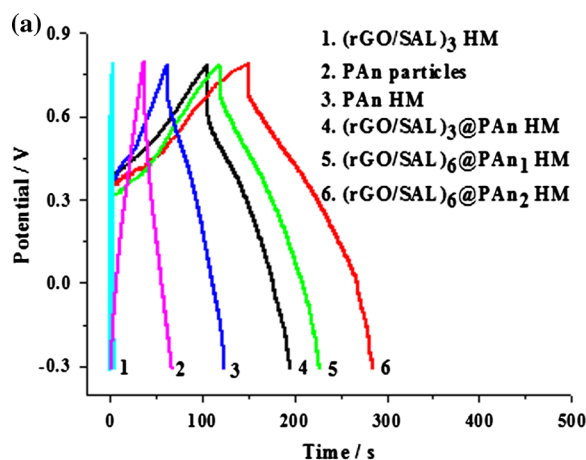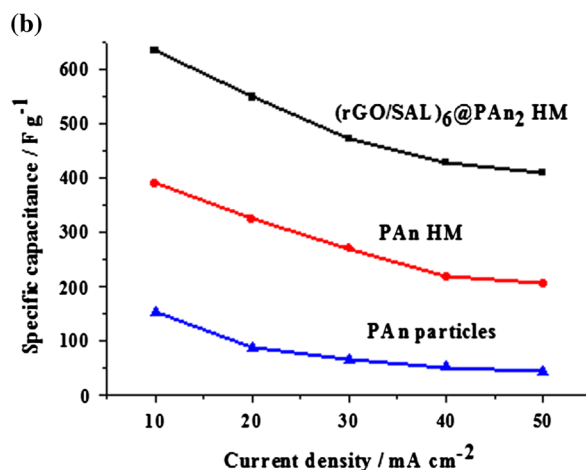
Fig. 6 Galvanostatic charge–discharge curves of PAn particles, PAn HM, (rGO/SAL)$_3$/PAn HM, (rGO/SAL)$_6$/PAn$_1$ HM, and (rGO/SAL)$_6$/PAn$_2$ HM electrodes at a current density of

10 mA cm^{-2} in 1.0 M H$_2$SO$_4$ solution. **b** Plots of specific capacitance for PAn particles, PAn HM, and (rGO/SAL)$_6$/PAn$_2$ HM electrodes at various current densities

(152 F g^{-1}) and (rGO/SAL)$_3$ HM 16 F g^{-1}). It might be attributed to the following factors. Firstly, the synergistic effect between rGO and PAn of hybrid shell could effectively increase the specific capacitance compared with the single component (Chen et al. 2011b; Cao et al. 2012). Secondly, the unique hollow structure is more favorable to simultaneously take place the redox reaction in the surface and interior of the materials, which can improve the electrochemical activity of PAn. Thirdly, the electron and ion more easily diffuse and migrate in the interior of hollow microspheres, which is advantageous to increase the utilization of electroactive materials of hybrid shell (Wu et al. 2010; Liu et al. 2008). Furthermore, the energy density of PAn particles, PAn HM, (rGO/SAL)$_3$ HM, (rGO/SAL)$_3$/PAn HM, (rGO/SAL)$_6$/PAn$_1$ HM, and (rGO/SAL)$_6$/PAn$_2$ HM can be calculated to be 91.96, 235.35, 9.68, 319.44, 380.55, and 382.97 Wh kg^{-1} at a current density of 10 mA cm^{-2}, respectively.

The rate performance of the (rGO/SAL)$_6$/PAn$_2$ HM, pure PAn particles, PAn HM electrode materials is evaluated by charging/discharging at different current densities. As shown in Fig. 6b, all the electrode materials exhibited a decreased capacitance retention at high current density, suggesting an increase in the diffusion resistance of electrolyte ions in the electrode materials (Korenblit et al. 2010). The (rGO/SAL)$_6$/PAn$_2$ HM electrode materials show an improved rate performance with 65 % capacitance

Table 1 Comparison of specific capacitances of the reported carbon-pseudocapacitance hybrid electrode materials with hollow structures and the present work

Samples	C_m/F g^{-1}	Ref.
Polyaniline/carbon black hybrid hollow microspheres	532 (−0.3–0.8 V, 10 mA cm^{-2})	Mu et al. (2013)
Polyaniline hollow spheres @electrochemical reduced graphene oxide hybrids	614 (0–0.8 V, 1.0 A g^{-1})	Fan et al. (2013)
Reduced graphene oxide– MnO$_2$ hollow sphere	578 (−0.7–0.3 V, 0.5 A g^{-1})	Chen et al. (2012)
Hollow carbon spheres-polyaniline composites	525 (−0.2–0.8 V, 0.1 A g^{-1})	Lei et al. (2010)
Graphene/polyaniline hollow microspheres	633 (−0.3–0.8 V, 10 mA cm^{-2})	This work

maintained as current density increases from 10 to 50 mA cm^{-2}, while the PAn HM remains about 53 % of its capacity in the same current density range. However, it retained only about 29 % compared with the specific capacitance at the current density of 10 mA cm^{-2} for the PAn particles. This might be attributed to the agglomeration of PAn particles owing to the higher surface energy, which hinders the access and diffusion of the electrolyte ions to the electrode surface. Thus, electrolyte ions are not easy to close to the active sites of PAn layers and a reduced contribution of pseudo-capacitance from the redox reaction of PANI at the interface of the electrolyte/electrode.
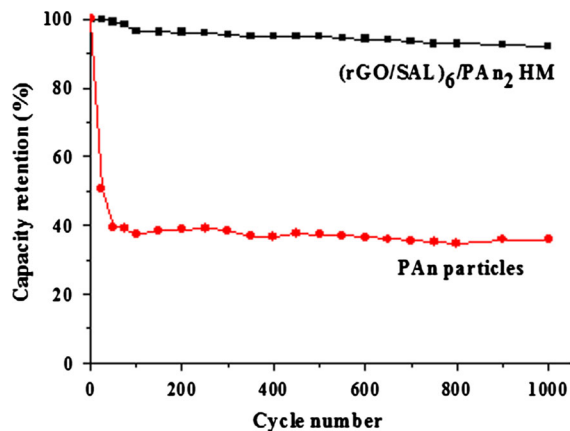
Fig. 7 Capacity retention with cycle number for the (rGO/SAL)$_6$/PAn$_2$ HM and PAn particles electrodes at a scan rate of 80 mV s^{-1} in 1.0 M H$_2$SO$_4$ solution

Furthermore, a detailed comparison indicates that the specific capacity of the (rGO/SAL)$_6$/PAn$_2$ HM in the present work is much higher than those of carbon-pseudocapacitance hybrid electrode materials with hollow structures in previous reports, as shown in Table 1.

Cycling stability is a key factor in determining the supercapacitor electrodes for many practical applications. It is also undoubted that excellent cycling performance is crucial for real supercapacitor application. The long-term cycle stability of the (rGO/SAL)$_6$/PAn$_2$ HM and PAn particles electrode materials was also tested by continuous cyclic voltammetric scans at the scan rates of 80 mV s^{-1} for 1,000 cycles in 1 M H$_2$SO$_4$ solution as shown in Fig. 7. PAn usually suffers from a poor long-term stability during cycling because the swelling and shrinking of PAn may lead to degradation (Li et al. 2011b, c). The terrible poor stability of the specific capacitance during cycling is observed for PAn particles. The capacitance retention rate is only 35.9 % after 1,000 cycles. Therefore, the instability of the capacitors based on PAn during long-term charge/discharge cycling is one of their most lethal deficiencies. However, the stability of PAn electrode materials can be largely improved by constructing the hybrid materials with hollow structure. It can be found that the (rGO/SAL)$_6$/PAn$_2$ HM electrode materials maintain 92 % of its original specific capacitance after 1,000 cycles. The improved electrochemical stability of the (rGO/SAL)$_6$/PAn$_2$ can be ascribed to the

introduction of rGO and can effectively relieve the contraction/expansion of PAn during doping/dedoping processes. Therefore, the graphene sheets can provide dual functions for improving the electrical conductivity and the stability of electrodes. In other words, the as-prepared (rGO/SAL)$_6$/PAn$_2$ HM electrode materials have got good cycle stability.

Electrochemical impedance spectroscopy (EIS) analysis is a powerful technique to evaluate the properties of conductivity, structure, and charge transport in the film/electrolyte interface. To obtain more information about the ability of rGO/PAn HM to function as electrodes in supercapacitors, an EIS measurement was carried out in a 1.0 M H$_2$SO$_4$ solution at 0.4 V (vs. SCE), as shown in Fig. 8. All of the Nyquist plots are semicircular over the high frequency range and are linear in the low frequency section. The intercept for the real component at the beginning of the semicircle shows the combined series resistance of the electrolyte, electrode, current collectors, and the electrode/current collector contact resistance (Kwon et al. 2013). The intersection of the curves at the real axis in the range of high-frequency region represents the effctive internal resistance (Rs), which is mainly attributed to the uncompensated solution resistance. It can be seen that Rs of PAn particles, PAn HM, (rGO/SAL)$_3$ HM, (rGO/SAL)$_3$/PAn HM, (rGO/SAL)$_6$/PAn$_1$ HM, and (rGO/SAL)$_6$/PAn$_2$ HM is 7.1, 9.9, 12.9, 9.0, 11.0, and 6.6 Ω, respectively. It can be inferred that the Rs of (rGO/SAL)$_6$/PAn$_2$ is smallest, in which the unique hybrid hollow structure can facilitate the efficient access of the electrolyte ions to the electrode surface and shorten the ion diffusion path. The Nyquist plots of impedance expresses a capacitive reactance arc, and the semicircle of capacitive reactance arc represents charge-transfer process (middle frequency) and the migration of the ions (high frequency). It could be seen that the diameter of the capacitive reactance arc of PAn nanoparticles, PAn HM, (rGO/SAL)$_3$/PAn HM, (rGO/SAL)$_6$/PAn$_1$ HM, and (rGO/SAL)$_6$/PAn$_2$ HM is approximately 31, 52, 50, 35, and 30 Ω, respectively. The electrical conductivities of PAn particles, PAn HM, (rGO/SAL)$_3$/PAn HM, (rGO/SAL)$_6$/PAn$_1$ HM, and (rGO/SAL)$_6$/PAn$_2$ HM are 1.02, 0.054, 0.007, 0.05, and 0.08 s cm^{-1}, respectively. It can be seen that the diameter of semicircular is decreased with the increase in the electrical conductivity of hybrid composites. It also indicated that the specific
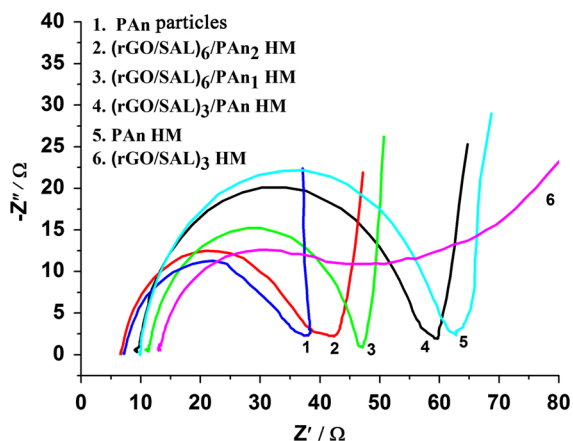
Fig. 8 Impedance Nyquist plots for PAn particles, PAn HM, (rGO/SAL)$_3$/PAn HM, (rGO/SAL)$_6$/PAn$_1$ HM, and (rGO/SAL)$_6$/PAn$_2$ HM electrodes

capacitance of (rGO/SAL)$_6$/PAn$_2$ HM was superior to that of others. At the low frequencies, the imaginary part of the impedance spectra represents the capacitive behavior of the electrode. The vertical line at the very low frequencies is caused by the accumulation of ions at the bottom of the pores of the electrode. The almost vertical line indicates good capacitive behavior without diffusion limitation (Mao et al. 2012). The straight line part of the curves except that of (rGO/SAL)$_3$ HM is closed to vertical line along the imaginary axis, suggesting that rGO/PAn HM have better capacitive behavior.

Conclusions

An effective strategy was developed for the fabrication of the graphene/polyanilin hybrid e hollow microspheres with an inner diameter about 2.0 μm using LBL technique and in situ chemical oxidative polymerization. The electrochemical tests showed that the specific capacitance of (rGO/SAL)$_6$/PAn$_2$ HM could reach about 633 F g^{-1} in a 1.0 M H$_2$SO$_4$ electrolyte. Furthermore, the obtained (rGO/SAL)$_6$/PAn$_2$ HM electrode materials have a good cycling stability with 92 % of its original specific capacitance after 1,000 cycles by continuous cyclic voltammetric scans at 80 mV s^{-1}. The greatly enhanced specific capacitance is ascribed to the unique hollow structure and the synergistic effect of the hybrid components of rGO and PAn, which favors the fast diffusion and

transport of electronic or ion and generates simultaneously double-layer capacitance and faradaic pseudocapacitance. Therefore, the graphene/polyaniline hybrid hollow microspheres with high apecific capacitance and good cycling stability are expected to be promising electrode materials to design high-performance supercapacitors.

References

Angelatos AS, Katagiri K, Caruso F (2006) Bioinspired colloidal systems via layer-by-layer assembly. Soft Matter 2:18–23

Ariga K, Hill JP, Ji QM (2007) Layer-by-layer assembly as a versatile bottom-up nanofabrication technique for exploratory research and realistic application. Phys Chem Chem Phys 9:2319–2340

Balducci A, Dugas R, Taberna P, Simon P, Plee D, Mastragostino M, Passerini S (2007) High temperature carbon–carbon supercapacitor using ionic liquid as electrolyte. J Power Sources 165:922–927

Bose S, Kuila T, Mishra AK, Rajasekar R, Kim NH, Lee JH (2012) Carbon-based nanostructured materials and their composites as supercapacitor electrodes. J Mater Chem 22:767–784

Cao JY, Wang YM, Zhou Y, Jia DC, Ouyang J-H, Guo LX (2012) Performances of high voltage electrochemical capacitor using ball-milled graphite/Mn$_3$O$_4$ composite electrodes. J Electroanal Chem 682:23–28

Caruso F (2000) Hollow capsule processing through colloidal templating and self-assembly. Chem Eur J 6:413–419

Chen JS, Wang ZY, Dong XC, Chen P, Lou XW (2011a) Graphene-wrapped TiO$_2$ hollow structures with enhanced lithium storage capabilities. Nanoscale 3:2158–2161

Chen XC, Kierzek K, Jiang ZW, Chen HM, Tang T, Wojtoniszak M, Kalenczuk RJ, Chu PK (2011b) Synthesis, growth mechanism, and electrochemical properties of hollow mesoporous carbon spheres with controlled diameter. J Phys Chem C 115:17717–17724

Chen H, Zhou SX, Chen M, Wu LM (2012) Reduced grapheme oxide-MnO$_2$ hollow sphere hybrid nanostructures as high-performance electrochemical capacitors. J Mater Chem 22:25207–25216

Chiou NR, Epstein AJ (2005) Polyaniline nanofibers prepared by dilute polymerization. Adv Mater 17:1679–1683

Chiou NR, Lee LJ, Epstein AJ (2007) Self-assembled polyaniline nanofibers/nanotubes. Chem Mater 19:3589–3591

Dong H, Prasad S, Nyame V, Jones WE Jr (2004) Submicrometer conducting polyaniline tubes prepared from polymer fiber templates. Chem Mater 16:371–373

Etacheri V, Marom R, Elazari R, Salitra G, Aurbach D (2011) Challenges in the development of advanced Li-ion batteries: a review. Energy Environ Sci 4:3243–3262

Fan W, Zhang C, Tjiu WW, Pramoda KP, He CB, Liu TX (2013) Graphene-wrapped polyaniline hollow spheres as novel hybrid electrode materials for supercapacitor applications. ACS Appl Mater Interfaces 5:3382–3391

Hadjipaschalis I, Poullikkas A, Efthimiou V (2009) Overview of current and future energy storage technologies for electric power applications. Renew Sustain Energy Rev 13:1513–1522

Han Y, Dong XT, Zhang C, Liu SX (2012) Hierarchical porous carbon hollow-spheres as a high performance electrical double-layer capacitor material. J Power Sources 211:92–96

Hong JK, Char KK, Kim BS (2010) Hollow capsules of reduced graphene oxide nanosheets assembled on a sacrificial colloidal particle. J Phys Chem Lett 1:3442–3445

Huang JX, Virji S, Weiller BH, Kaner RB (2003) Polyaniline nanofibers: facile synthesis and chemical sensors. J Am Chem Soc 125:314–315

Huang CJ, Hong CW, Ko FH, Chang FC (2011) Fabrication of vesicle-like dual-responsive click capsules by direct covalent layer-by-layer assembly. Soft Matter 7:10850–10855

Jang J, Yoon H (2003) Facile fabrication of polypyrrole nanotubes using reverse microemulsion polymerization. Chem Commun 6:720–721

Jiang H, Ma J, Li CZ (2012) Polyaniline-MnO_2 coaxial nanofiber with hierarchical structure for high-performance supercapacitors. J Mater Chem 22:16939–16942

Kamat PV (2007) Meeting the clean energy demand: nanostructure architectures for solar energy conversion. J Phys Chem C 111:2834–2860

Kim MJ, Hwang YS, Kim JH (2013) Graphene/MnO_2-based composites reduced via different chemical agents for supercapacitors. J Power Sources 239:225–233

Korenblit Y, Rose M, Kockrick E, Borchardt L, Kvit A, Kaskel S, Yushin G (2010) High-rate electrochemical capacitors based on ordered mesoporous silicon carbide-derived carbon. ACS Nano 4:1337–1344

Kovtyukhova NI, Ollivier PJ, Martin BR, Mallouk TE, Chizhik SA, Buzaneva EV, Gorchinskiy AD (1999) Layer-by-layer assembly of ultrathin composite films from micron-sized graphite oxide sheets and polycations. Chem Mater 11:771–778

Kwon OS, Kim TJ, Lee JS, Park SJ, Kang MJ, Lee JE, Jang JS, Yoon HS (2013) Fabrication of graphene sheets intercalated with manganese oxide/carbon nanofibers: toward high-capacity energy storage. Small 9:248–254

Lai XY, Halperta JE, Wang D (2012) Recent advances in micro-/nano-structured hollow spheres for energy applications: from simple to complex systems. Energy Environ Sci 5:5604–5618

Lei ZB, Chen ZW, Zhao XS (2010) Growth of polyaniline on hollow carbon spheres for enhancing electrocapacitance. J Phys Chem C 114:19867–19874

Li GC, Li YM, Li Y, Peng HR, Chen KZ (2011a) Polyaniline nanorings and flat hollow capsules synthesized by in situ sacrificial oxidative templates. Macromolecules 44:9319–9323

Li J, Xie HQ, Li Y, Liu J, Li ZX (2011b) Electrochemical properties of graphene nanosheets/polyaniline nanofibers composites as electrode for supercapacitors. J Power Sources 196:10775–10781

Li Y, Zhao X, Xu Q, Zhang Q, Chen D (2011c) Facile preparation and enhanced capacitance of the polyaniline/sodium alginate nanofiber network for supercapacitors. Langmuir 27:6458–6463

Li LY, Xia KQ, Li L, Shang SM, Guo QZ, Yan GP (2012) Fabrication and characterization of free-standing polypyrrole/graphene oxide nanocomposite paper. J Nanopart Res 14:908

Liu R, Cho SI, Lee SB (2008) Poly(3,4-ethylenedioxythiophene) nanotubes as electrode materials for a high-powered supercapacitor. Nanotechnology 19:215710

Lou XW, Archer LA, Yang ZC (2008) Hollow micro-/nano-structures: synthesis and applications. Adv Mater 20:3987–4091

Mao L, Zhang K, Chan H, Wu J (2012) Nanostructured MnO_2/grapheme composites for supercapacitor electrodes: the effect of morphology, crystallinity and composition. J Mater Chem 22:1845–1851

Mu B, Liu P, Li XR, Du PC, Dong Y, Wang YJ (2012) Fabrication of flocculation-resistant pH/ionic strength/temperature multiresponsive hollow microspheres and their controlled release. Mol Pharm 9:91–101

Mu B, Liu P, Wang AQ (2013) Synthesis of polyaniline/carbon black hybrid hollow microspheres by layer-by-layer assembly used as electrode materials for supercapacitors. Electrochim Acta 88:177–183

Park MK, Onishi K, Locklin J, Caruso F, Advincula RC (2003) Self-assembly and characterization of polyaniline and sulfonated polystyrene multilayer-coated colloidal particles and hollow shells. Langmuir 19:8550–8554

Peyratout CS, Dähne L (2004) Tailor-made polyelectrolyte microcapsules: from multilayers to smart containers. Angew Chem Int Ed 43:3762–3783

Shi J, Chen Z, Qin Y, Guo ZX (2008) Multiwalled carbon nanotube microspheres from layer-by-layer assembly and calcination. J Phys Chem C 112:11617–11622

Stejskal J, Kratochvíl P, Radhakrishnan N (1993) Polyaniline dispersions 2 UV-vis absorption spectra. Synth Metals 61:225–231

Tang MX, Qin YJ, Wang YY, Guo ZX (2009) Hollow carbon nanotube microspheres and hemimicrospheres. J Phys Chem C 113:1666–1671

Wu Q, Xu YX, Yao ZY, Liu A, Shi GQ (2010) Supercapacitors based on flexible graphene/polyaniline nanofiber composite films. ACS Nano 4:1963–1970

Yu AQ, Park HW, Davies A, Higgins DC, Chen ZW, Xiao XC (2011a) Free-standing layer-by-layer hybrid thin film of graphene-MnO_2 nanotube as anode for lithium ion batteries. J Phys Chem Lett 2:1855–1860

Yu GH, Hu LB, Liu N, Wang HL, Vosgueritchian M, Yang Y, Cui Y, Bao Z (2011b) Enhancing the supercapacitor performance of graphene/MnO_2 nanostructured electrodes by conductive wrapping. Nano Lett 11:4438–4442

Zhang J, Kong LB, Cai JJ, Luo YC, Kang L (2010a) Nanocomposite of polypyrrole/modified mesoporous carbon for electrochemical capacitor application. Electrochim Acta 55:8067–8073

Zhang K, Zhang LL, Zhao XS, Wu JS (2010b) Graphene/polyaniline nanofiber composites as supercapacitor electrodes. Chem Mater 22:1392–1401

Zhong CJ, Luo J, Njoki PN, Mott D, Wanjala B, Loukrakpam R, Lim S, Wang LY, Fang B, Xu ZC (2008) Fuel cell

technology: nano-engineered multimetallic catalysts. Energy Environ Sci 1:454–466

Zhu YW, Murali ST, Stoller MD, Ganesh KJ, Cai WW, Ferreira PJ, Pirkle A, Wallace RM, Cychosz KA, Thommes M, Su D, Stach EA, Ruoff RS (2011) Carbon-based supercapacitors produced by activation of graphene. Science 332:1537–1541

Zolfaghari A, Naderi HR, Mortaheb HR (2013) Carbon black/manganese dioxide composites synthesized by sono-chemistry method for electrochemical supercapacitors. J Electroanal Chem 697:60–67